GEOPHYSICS, VOL. 79, NO. 5 (SEPTEMBER-OCTOBER 2014); P. D319–D331, 15 FIGS., 3 TABLES.
10.1190/GEO2013-0438.1



# The effect of surface roughness and mixed-mode loading on the stiffness ratio $\kappa_x/\kappa_z$ for fractures

Min-Kwang Choi[1], Antonio Bobet[2], and Laura J. Pyrak-Nolte[3]

## ABSTRACT

The characterization of fractures using elastic waves requires a parameter that captures the physical properties of a fracture. Many theoretical and numerical approaches for wave propagation in fractured media use normal and shear fracture specific stiffness to represent the complexity of fracture topology as it deforms under stress. Most effective medium approaches assume that the normal and shear fracture specific stiffness are equal, yielding a shear-to-normal specific stiffness ratio of one. Yet several experimental studies show that this ratio can vary from zero to three. We conducted a series of experiments to determine the stiffness ratio for fractures with different surface roughness subjected to mixed-mode loading conditions. Specimens containing a single fracture were subjected to either normal loading or combined normal and shear loading during ultrasonic measurements of transmitted and reflected P- and S-waves. Theoretical analysis based on the displacement discontinuity theory shows, for P- and S-waves with the same wavelength, that the theoretical stiffness ratio is not equal to one, but depends on the ratio of S- to P-wave velocities. The conventional stiffness ratio limit of unity is determined to be appropriate for very smooth fracture surfaces even under mixed-mode loading conditions. However, rough fracture surfaces result in stiffness ratios that are greater than the theoretical limit and the magnitude of the ratio depended on the relative ratio of shear-to-normal stress. The results from the experiments suggest that the conventional practice of assuming a constant stiffness ratio equal to 1.0 may not be appropriate. Therefore, the ratio of shear-to-normal fracture specific stiffness depends on the roughness of the fracture surface and the loading conditions.

## INTRODUCTION

Numerical and theoretical studies of seismic wave propagation in fractured media require inclusion of a parameter that describes the physical properties of fractures. The physical properties of a fracture include geometric properties such as surface roughness and length, as well as the size and spatial distribution of contact area and fracture apertures. For materials with multiple fractures, additional information on the number/density of fractures, fractures spacing, and orientation would also be included. For a single macroscopic through going fracture, the complexity of fracture geometry is captured by fracture specific stiffness $\kappa$. Fracture specific stiffness, also known as unit joint stiffness, was introduced by Goodman et al. (1968) to describe the behavior of a fracture because it could be measured in the laboratory without detailed analysis of the fracture geometry. When a rock containing a fracture is stressed, the measured deformation includes deformation of the rock matrix and the fracture (Hopkins, 1990). By measuring displacements across equal lengths of the rock matrix and across the fracture for a range of stresses, the fracture displacement can be obtained by subtraction of these two measurements. The slope of the stress-fracture displacement curve is defined as the fracture specific stiffness, has units of a force per volume, and captures the effect of the additional deformation that arises from the presence of a fracture. In fact, fracture specific stiffness represents the relationship between an increment in stress and the resulting additional deformation of the fracture. Many studies have measured normal fracture specific stiffness $\kappa_z$ using this approach and demonstrated that the fracture stiffness exhibits a nonlinear relationship with stress; i.e., fracture-specific stiffness is a function of applied stress (Hopkins et al., 1987; Pyrak-Nolte et al., 1987; Jaeger et al., 2007; Lubbe et al., 2008; Far, 2011).

Manuscript received by the Editor 24 November 2013; revised manuscript received 6 April 2014; published online 13 August 2014.
[1]Samsung C&T, Seoul, Korea. E-mail: minkwang.choi@gmail.com.
[2]Purdue University, School of Civil Engineering, West Lafayette, Indiana, USA. E-mail: bobet@ecn.purdue.edu.
[3]Purdue University, Department of Physics and Astronomy; Department of Earth, Atmospheric and Planetary Sciences; and School of Civil Engineering, West Lafayette, Indiana, USA. E-mail: ljpn@purdue.edu.

Of particular interest for theoretical and numerical approaches to understanding seismic wave propagation through fractured media is the ratio of shear-to-normal stiffness $\kappa_x/\kappa_z$ or the ratio of normal to shear compliance $B_N/B_T$. Although normal fracture specific stiffness is easily measured using the experimental approach described above, measurements of shear fracture specific stiffness $\kappa_x$ are more complicated because selecting a measurement length scale for the rock matrix and fracture is not trivial. Another approach used to determine normal and shear fracture specific stiffness is from the measurements of seismic/ultrasonic waves propagated through fractured rock. This approach has been used on a wide range of scales to obtain normal and shear stiffness at the grain scale (microcracks) in cored samples (Sayers, 1999; Sayers and Han, 2002; MacBeth and Schuett, 2007; Verdon et al., 2008; Angus et al., 2009; Pervukhina et al., 2011), for synthetic fractures at the laboratory scale (Hsu and Schoenberg, 1993; Rathore et al., 1995; Far, 2011; Far et al., 2014), on single fractures at laboratory scale (Pyrak-Nolte et al., 1990; Lubbe et al., 2008; Shao and Pyrak-Nolte, 2013), and field-scale fractures (Hobday and Worthington, 2012; Verdon and Wüstefeld, 2013).

The expected value of the ratio of shear-to-normal stiffness is often based on mechanical models that represent a fracture as either a planar distribution of small isolated areas of slip (cracks) (Hudson, 1981; Hsu and Schoenberg, 1993; Sayers and Kachanov, 1995; Liu et al., 2000; Gueguen and Schubnel, 2003; Levin and Markov, 2004; Grechka, 2007; Kachanov et al., 2010) or as a planar distribution of imperfect interfacial contacts (Johnson, 1985; Hudson, 1997; Liu et al., 2000; Kachanov et al., 2010). For the case in which a fracture is modeled as a planar distribution of small isolated areas of slip, a fracture is represented as a collection of open penny-shaped geometries with a radius $a$, in an isotropic material with the Poisson's ratio $\nu$, and Young's modulus E. The normal and shear compliances ($B_N$ and $B_T$) are given by (Rice, 1979)

$$B_N = 16(1-\nu^2)\frac{a}{3\pi E}, \tag{1}$$

$$B_T = 32(1-\nu^2)\frac{a}{3\pi E(2-\nu)} = \frac{B_N}{1-\nu/2}. \tag{2}$$

The compliance ratio $B_N/B_T$ is

$$\frac{B_N}{B_T} = 1-\frac{\nu}{2} = \frac{\kappa_x}{\kappa_z}. \tag{3}$$

Here, the compliance ratio $B_N/B_T$ is equivalent to the ratio of shear ($\kappa_x$) to normal ($\kappa_z$) fracture specific stiffness $\kappa_x/\kappa_z$ (Schoenberg, 1980).

Sayers and Kachanov (1995) propose a fundamental formulation to estimate fracture compliance when a fracture consisted of a planar distribution of small isolated areas of slip (cracks). Assuming that the interaction between cracks is small enough to be taken as negligible, the average vector $u_i$ at a displacement discontinuity (fracture) can be given in terms of the average traction $t_i$, applied at the crack:

$$[u_i] = B_{ij}t_j = B_{ij}\sigma_{jk}n_k, \tag{4}$$

where $\sigma_{jk}$ is the applied stress and $n_k$ is the $k$th component of unit vector that is normal to the surface of the crack. Here, the crack compliance tensor $B_{ij}$ is represented as the sum of the normal and shear compliances ($B_N$ and $B_T$):

$$B_{ij} = B_N n_i n_j + B_T(\delta_{ij} - n_i n_j), \tag{5}$$

where $\delta_{ij}$ is the Kronecker delta. The compliance tensor $\Delta S_{ijkl}$ caused by the existence of cracks is defined as

$$\Delta S_{ijkl} = \frac{1}{4}(\delta_{ik}\alpha_{jl} + \delta_{il}\alpha_{jk} + \delta_{jk}\alpha_{il} + \delta_{jl}\alpha_{ik}) + \beta_{ijkl}, \tag{6}$$

$$\alpha_{ij} = \frac{1}{V}\sum_r B_T^r n_i^r n_j^r A^r, \tag{7}$$

$$\beta_{ijkl} = \frac{1}{V}\sum_r (B_N^r - B_T^r) n_i^r n_j^r n_k^r n_l^r A^r. \tag{8}$$

Here, $r$ is the number of planar discontinuities with crack area $A^r$ and $V$ is a volume element. Note that the values of $\alpha_{ij}$ and $\beta_{ijkl}$ depend only on the values of the indices, but not on their order, e.g., $\beta_{1122} = \beta_{1212}$ and $\beta_{1133} = \beta_{1313}$, etc. Equations 6–8 consider the distribution of crack orientations by specifying $\alpha_{ij}$ and $\beta_{ijkl}$. Sayers and Kachanov (1995) predicted that, if $B_N$ is equal to $B_T$ for all cracks, $\beta_{ijkl}$ goes to zero and $\Delta S_{ijkl}$ depends only on the second-rank tensor $\alpha_{ij}$. This case corresponds to a transversely isotropic material with the axis of orthotropy coinciding with the principal axes of $\alpha_{ij}$. Kachanov (1980) and Sayers (1991) also showed that the compliance tensor $B_{ij}$ has orthotropic symmetry, i.e., three orthogonal planes of mirror symmetry, if $B_N = B_T$.

Alternatively, a fracture can be assumed as a collection of a planar distribution of imperfect interfacial contacts (Johnson, 1985; Hudson et al., 1997; Liu et al., 2000; Kachanov et al., 2010). Johnson (1985) derives equations 9 and 10 that calculate total pressures that generate unit indentation in normal ($B_N$) and tangential ($B_T$) directions on a circular region of radius $b$ on the surface of an elastic half space. The equations are

$$B_N = \frac{-4(\lambda+\mu)}{(\lambda+2\mu)} \tag{9}$$

and

$$B_T = \frac{-8(\lambda+\mu)}{(3\lambda+4\mu)}, \tag{10}$$

where $\mu$ and $\lambda$ are the Lamé's constants.

Hudson et al. (1997) modeled a fracture as two rough surfaces based on a random distribution of circular contacts and derived the equations for normal and shear stiffness. Worthington and Hudson (2000) modified the equations of Hudson et al. (1997) to include the effect of material filling the void spaces of a fracture. Worthington and Hudson (2000) defined the normal and shear stiffnesses as follows:

$$\kappa_z = r^w\frac{4\mu}{\pi a}\left(1-\frac{V_S^2}{V_P^2}\right)\left\{1+\frac{2(r^w)^{1/2}}{\sqrt{\pi}}\right\} + \frac{K' + \frac{4}{3}\mu'}{\Delta} \tag{11}$$

and

$$\kappa_x = r^w \frac{8\mu}{\pi a}\left(1-\frac{V_S^2}{V_P^2}\right)\left\{1+\frac{2(r^w)^{1/2}}{\sqrt{\pi}}\right\}\Big/\left(3-\frac{2V_S^2}{V_P^2}\right)+\frac{\mu'}{\Delta}, \tag{12}$$

where $V_P$ and $V_S$ are the P- and S-wave velocities, respectively, and μ is the Lamé's constant. Here, $r^w$ is the proportion of the fracture surface area that is in contact, $a$ is the mean radius of the contact areas, $\mu'$ and $K'$ are the Lamé's constant and bulk modulus of the fracture fill, and $\Delta$ is the mean aperture of the fracture. If a fracture is dry (e.g., a gas-filled fracture) the second term in equations 11 and 12, which are related to the fracture filling material, are negligible.

In summary, for the case of a planar distribution of small isolated areas of slip, the stiffness ratio $\kappa_x/\kappa_z$ is equal to $(1-\nu/2)$. If a fracture is assumed to be a planar distribution of imperfect interfacial contacts, the ratio $\kappa_x/\kappa_z$ is given by the expression $(1-\nu)/(1-\nu/2)$. Both cases give a value of ∼1.0 for $\kappa_x/\kappa_z$ because Poisson's ratio for rock ranges typically from $0.1 \le \nu \le 0.4$ (Gercek, 2007).

Although theoretically it has been shown that the value of $\kappa_x/\kappa_z \approx 1$, laboratory and field scale experiments have measured values that range from 0.05 to 3.0. At the grain scale, several studies used ultrasonic measurements to determine fracture stiffness of the microcracks in a rock matrix. Sayers (1999) and Sayers and Han (2002) obtained ratios varying from 0.25 to 3.0 for sandstones and shale samples when the samples were dry, while the ratio dropped to 0.05 to 1.1 when the samples were saturated with water. MacBeth and Schuett (2007) investigate the stiffness ratio when a sample was thermally damaged. A stiffness ratio of the undamaged sample was measured first and then after damage from heating. They found that for the undamaged sample, the ratio ranged from 0 to 0.6 and after damage ranged from 0 to 1.2. They concluded that heating the diagenetic infilling in the preexisting microcracks in the rock induced an increase in the stiffness ratio.

Verdon et al. (2008) found a ratio of $0.68 < \kappa_x/\kappa_z < 1.06$ for a sandstone sample from the Clair oil field tested under dry conditions. Angus et al. (2009) estimated the ratio to be between 0.25 and 1.5 from ultrasonic-wave measurements for a sandstone sample. Pervukhina et al. (2011) obtained stiffness ratios of 0–2.0 on various types of shale recovered from depths between 200 and 3604 m. In summary, the results of the experiments carried on cracks at the grain scale do not agree with the conventional assumption that $\kappa_x/\kappa_z \approx 1.0$.

Hsu and Schoenberg (1993) created a synthetic fracture made of multiple Lucite plates and determine a ratio of 0.8–1.0 for dry conditions, but found values less than 0.1 when the fracture was saturated with honey. Far (2011) also made a block composed of multiple Lucite plates and measured a ratio of 0.11–0.76 for dry conditions. When filling the fracture with rubber pellets, the stiffness ratio increased to 1.6. Rathore et al. (1995) created a synthetic fracture with cementing sand. A known distribution of cracklike features was created by including metal disks. The metal disks were removed after the sample was solidified leaving behind crack like voids. P- and S-wave velocities were measured across the synthetic fracture from which Verdon and Wüstefeld (2013) computed a $B_N/B_T$ ratio of 0.46.

Far et al. (2014) investigated the effect of frequency, stress, and inclusions on fracture compliance. Ultrasonic measurements were made on two Plexiglas samples composed of multiple plates with and without inclusions of rubber disks. For the fractures without the rubber inclusions, the stiffness ratios increased from 0.4 to 0.9 and from 0.1 to 0.53 at low (90/120 kHz) and high frequencies (431/480 kHz), respectively, as the normal stress increased up to 14.59 MPa. However, when the rubber disks were inserted into the fractures, the stiffness ratios at the low and high frequency were reduced to 0.25–0.1 and <0.14, respectively.

Lab-scale data on single natural or synthetic fractures are limited. Pyrak-Nolte et al. (1990) measure the normal and shear fracture stiffness of natural fractures on three cored samples of quartz monzonite for normal stresses up to 85 MPa. Based on their published data, the estimated ratio of shear-to-normal stiffness ranged from 0.2 to 0.7 when the rock was dry and from 0.04 to 0.5 when saturated. Lubbe et al. (2008) created synthetic fractures in limestone samples by placing two blocks of limestone in contact. Fracture roughness was controlled by grinding and/or polishing the two surfaces. They determined the stiffness ratio from ultrasonic measurements of P- and S-waves. The stiffness ratio ranged from 0.2 to 0.55 and dramatically decreased to 0.02–0.05 with honey saturation.

Hobday and Worthington (2012) and Verdon and Wüstefeld (2013) carried out field scale experiments to estimate the stiffness ratio. Hobday and Worthington (2012) obtained the ratio for a saturated outcrop of upper Caithness flagstone using hammer seismic techniques. The fracture spacing, in the field, was approximately 0.5 m. The estimated stiffness ratio was less than 0.1. Verdon and Wüstefeld (2013) applied S-wave splitting to downhole microseismic data and determined a stiffness ratio of 0.7–0.78 for dry conditions and a ratio of 1–2 during proppant injection.

Figure 1 summarizes the ratios of shear-to-normal fracture stiffness obtained from the aforementioned experimental studies. All data except the field scale experiment were obtained under normal compression only; i.e., no shear stress was applied to the fracture. It is clear from the figure that many of the results deviate from the theoretical estimate of $\kappa_x/\kappa_z = 1.0$, and it suggests that the common convention of assuming that $\kappa_x/\kappa_z = 1.0$ may not be appropriate. Based on the literature, there are several factors that may change or affect the stiffness ratio such as presence of filling material in the fracture (Pyrak-Nolte et al., 1990; Sayers, 1999; Sayers and Han, 2002; Grechka and Kachanov, 2006; Lubbe et al., 2008; Far, 2011), orientation of microcracks (Sayers and Kachanov, 1995; Liu et al., 2000; Pervukhina et al., 2011), partial contact of the surfaces (Grechka and Kachanov, 2006), thermal damage to rock matrix (MacBecth and Schuett, 2007), and mineralization of material (Sayers et al., 2009).

In this paper, a combined experimental and theoretical approach are taken to determined the effect of surface roughness and mixed-mode loading conditions on the $\kappa_x/\kappa_z$ ratio. A theoretical approach based on the displacement discontinuity theory is used to determine the theoretical limit of the $\kappa_x/\kappa_z$ ratio, which depends on the material properties of the matrix and the frequency of the signal. The experimental approach included laser profilometry to characterize the roughness of the fracture surfaces and an ultrasonic technique to measure transmitted and reflected P- and S-waves. The experimental value of the $\kappa_x/\kappa_z$ ratio is compared with the theoretical limit to determine if the loading condition and surface roughness of the fractures affect this ratio.

## THEORY

In this section, the theoretical approach used to determine the $\kappa_x/\kappa_z$ ratio is described. In this approach, the fracture is represented as a displacement discontinuity or linear slip interface. Transmission and reflection coefficients for waves propagated at normal incident to the fracture are used to determine the shear and normal stiffnesses as well as the ratio of $\kappa_x/\kappa_z$.

## Ratio of shear-to-normal specific stiffness

We determine the theoretical value of the $\kappa_x/\kappa_z$ ratio based on the seismic response of a single fracture to P- and S-waves. In this approach, the fracture is represented as a displacement discontinuity or linear-slip interface (Schoenberg, 1980, 1983; Pyrak-Nolte, 1988, 1996; Pyrak-Nolte et al., 1990) between two elastic half spaces. The boundary conditions that define the interface assume that the stresses across the interface are continuous but the displacements are not. The discontinuity in displacement is inversely proportional to the fracture specific stiffness. The fracture is represented by normal and shear specific stiffnesses. We refer the reader to Schoenberg (1980, 1983), Pyrak-Nolte (1988, 1996), or Pyrak-Nolte et al. (1990) for the full solution to the theory for wave propagation across a displacement discontinuity for various incident angles and material properties.

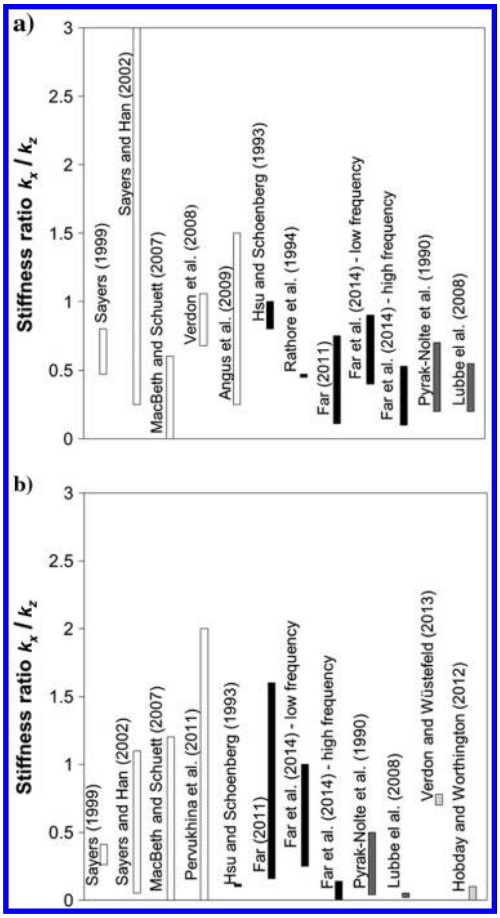


Figure 1. Ratio of shear-to-normal fracture specific stiffness (a) when a fracture is dry and (b) when it is saturated with fluid, filled with rubber, or thermally damaged. White bars are used for fractures at the grain scale, black for synthetic fractures at laboratory scale, dark gray for a single fracture at laboratory scale, and light gray for field-scale fractures (modified after Verdon and Wüstefeld, 2013).

Our experimental approach is based on measurements made at normal incidence to the fracture plane. The reflection and transmission coefficients for normal incidence (Pyrak-Nolte et al., 1990) from the displacement discontinuity theory are

$$R = \frac{-i\omega}{[-i\omega + 2(\kappa/Z)]} \tag{13}$$

and

$$T = \frac{2(\kappa/Z)}{[-i\omega + 2(\kappa/Z)]}, \tag{14}$$

where $\omega$ is the angular frequency and $Z$ is the seismic impedance (phase velocity of the half spaces times the density of the half spaces). The estimation of $\kappa_x$, the shear fracture specific stiffness, is based on the reflection and transmission coefficients for S-waves propagated at normal incidence to the fracture (and hence S-wave seismic impedance), whereas normal fracture specific stiffness $\kappa_z$ is based on the P-wave seismic impedance and the P-wave transmission and reflection coefficients. For a purely elastic medium, the reflection and transmission coefficients are frequency dependent and depend on the specific stiffness of the fracture. The frequency dependent response arises from the discontinuity in displacement across a fracture in an elastic medium.

Equation 14 can be rewritten to determine the fracture specific stiffness, namely

$$\kappa = \frac{\omega Z}{\sqrt{\frac{1}{T^2} - 1}}. \tag{15}$$

The S-wave impedance ($Z_\mathrm{S}$), transmission coefficient ($T_\mathrm{S}$), and signal frequency ($\omega_\mathrm{S}$) are used to determine $\kappa_x$, whereas the P-wave impedance ($Z_\mathrm{P}$), transmission coefficient ($T_\mathrm{P}$), and signal frequency ($\omega_\mathrm{P}$) are used to determine $\kappa_z$. Based on equation 15 and the relevant parameters, the ratio of shear-to-normal fracture specific stiffness is

$$\frac{\kappa_x}{\kappa_z} = \frac{\left(\omega_\mathrm{S} Z_\mathrm{S} / \sqrt{\frac{1}{T_\mathrm{S}^2} - 1}\right)}{\left(\omega_\mathrm{P} Z_\mathrm{P} / \sqrt{\frac{1}{T_\mathrm{P}^2} - 1}\right)} = \frac{\omega_\mathrm{S}(\rho V_\mathrm{S})}{\omega_\mathrm{P}(\rho V_\mathrm{P})} \frac{\sqrt{(1/T_\mathrm{P}^2) - 1}}{\sqrt{(1/T_\mathrm{S}^2) - 1}} = \frac{\omega_\mathrm{S} V_\mathrm{S}}{\omega_\mathrm{P} V_\mathrm{P}} f(T_\mathrm{P}, T_\mathrm{S}), \tag{16}$$

where

$$f(T_\mathrm{P}, T_\mathrm{S}) = \frac{\sqrt{\frac{1}{T_\mathrm{P}^2} - 1}}{\sqrt{\frac{1}{T_\mathrm{S}^2} - 1}}, \tag{17}$$

and where $\rho$ is the density of the medium, $V$ is the phase velocity, and $T$ is the transmission coefficient; subscripts S and P indicate S- and P-waves, respectively. The relative transmission of P- and S-waves is expressed as $f\,(T_\mathrm{P}, T_\mathrm{S})$ because it is not known a priori if the transmission across a fracture is the same for both waves. If the transmission of P- and S-waves across the fracture is the same; i.e., $T_\mathrm{P} \approx T_\mathrm{S}$, the function $f(T_\mathrm{P}, T_\mathrm{S}) \approx 1$ and equation 16 simplifies to

$$\frac{\kappa_x}{\kappa_z} = \frac{\omega_S}{\omega_P}\frac{V_S}{V_P} = \frac{\omega_S}{\omega_P}\sqrt{\frac{0.5-\nu}{1-\nu}}, \tag{18}$$

where $\nu$ is the Poisson's ratio. If a fracture is in a viscoelastic medium, equation 18 would have to also include the effects of velocity dispersion. However, for a fracture in an elastic medium as in this study, equation 18 implies that the specific stiffness ratio depends on frequency and the ratio of the intact S- to P-wave velocity, which is a function of Poisson's ratio. If the same frequencies are selected for S- and P-waves, i.e., $\omega_S = \omega_P$, the stiffness ratio reduces to the ratio of the S- to P-wave velocity. In this study, $\omega_S \neq \omega_P$ because the analysis is performed for values of $\omega_S$ and $\omega_P$ that yield the same wavelength (see Table 1 for values). Restricting the analysis to the same wavelength reduces the effect of any potential wavelength-dependent mechanisms.

If the stiffness ratio estimated from the experimental measurements deviates from the theoretical limit given by equation 18, then the function $f(T_P, T_S)$ is not equal to one. This means that a fracture affects the transmission of P- and S-waves differently for the same wavelength. When the ratio is less than the theoretical value, S-waves are more strongly attenuated or scattered by the fracture than P-waves. Conversely, when the stiffness ratio is greater than the theoretical value, S-waves are transmitted with relatively less attenuation than P-waves.

### Ratio of reflection to transmission coefficient

Fracture specific stiffness can be determined from transmitted and reflected waves by taking the ratio of the reflection coefficient to the transmission coefficient $R/T$, based on equations 13 and 14:

$$\left|\frac{R}{T}\right| = \frac{1}{2}\left|\frac{\omega Z}{\kappa}\right|. \tag{19}$$

As shown in equation 19, the $R/T$ ratio is linear with normalized frequency, $\omega Z/\kappa$. Hence, once $R/T$ is determined from the experimental data, the fracture specific stiffness $\kappa$ can be directly calculated from equation 19, if the seismic impedance $Z$, and angular frequency $\omega$ are known.

The transmission and reflection coefficients are shown as a function of the normalized frequency $\omega Z/\kappa$ in Figure 2 along with the ratio of $R/T$. Normalized frequency decreases with increasing fracture specific stiffness. As $\omega Z/\kappa$ decreases, the transmission coefficient increases while the reflection coefficient decreases. Interestingly, when the normalized frequency decreases from 15 to 4, the reflection coefficient only decreases by approximately 10%, whereas the transmission coefficient increases by a factor of 3.4. When the normalized frequency $\omega Z/\kappa < 4$, both the transmission and reflection coefficients are sensitive to changes in fracture specific stiffness. Based on this analysis, the transmission coefficient is more useful for detecting changes in fracture specific stiffness for normalized frequencies within the range of 0–15.

**Table 1. Frequency and wave velocity for Lucite and gypsum.**

| | Frequency (MHz) | | Wave velocity (m/s) | | Wavelength (mm) | |
|---|---|---|---|---|---|---|
| | P-wave | S-wave | P-wave | S-wave | P-wave | S-wave |
| Lucite | 1.00 | 0.50 | $2760 \pm 2$ | $1375 \pm 2$ | 2.8 | 2.8 |
| Gypsum | 0.67 | 0.40 | $3150 \pm 2$ | $1880 \pm 2$ | 4.7 | 4.7 |

## LABORATORY EXPERIMENT

In this section, the experimental methods used to determine the effect of loading and fracture surface roughness on the $\kappa_x/\kappa_z$ ratio are given. First, a description of the sample fabrication process is provided that details the method for generating surfaces with different roughness. Next, the approach for characterizing surface roughness is presented. Then the ultrasonic methods used to determine the $\kappa_x/\kappa_z$ ratio are described along with the loading conditions applied to the samples.

### Sample preparation

Synthetic fractures with mated and nonmated rough surfaces were created using either gypsum or acrylic (Lucite) to examine the effect of surface roughness and loading conditions on the ratio of shear-to-normal fracture specific stiffness. Gypsum was chosen because it has been used extensively for experimental simulations of rock with flaws or fractures (Reyes et al., 1991; Takeuchi, 1991; Hsu and Schoenberg, 1993; Shen et al., 1995; Bobet and Einstein, 1998; Ko et al., 2006; Wong and Einstein, 2006; Lubbe et al., 2008; Far, 2011) and was chosen for the ease of sample preparation.

A synthetic fracture in gypsum was created by placing sandpaper with a known grit size at the bottom of a mold. Table 2 lists the types of sandpaper used to control the size of the asperities and the names of specimens. The average grit size of the sandpaper increased from 68 to 530 μm. A mixture of gypsum was made that was composed of mass proportions of water/gypsum = 0.6 and water/diatomaceous earth = 35 (Bobet and Einstein, 1998). Diatomaceous earth prevents bleeding of water to the top of the specimen during fabrication. The gypsum was poured into the mold and the mold was then placed on a vibrating table and vibrated for 5 min to remove any entrapped air. After 75 min of hardening, the sand paper was removed and a second block was cast against the rough surface of the first block, creating a mated

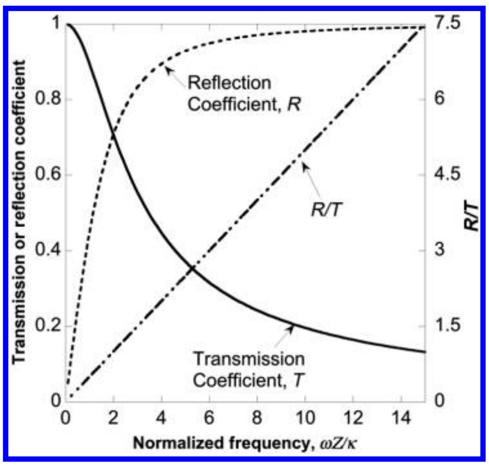


Figure 2. Transmission and reflection coefficients and ratio $R/T$ as a function of normalized frequency $\omega Z/\kappa$.

fracture. Before casting the second block, a release agent was applied to the contact surface to prevent the second block from sticking to the first block. After casting the second block for 75 min, the specimen was taken out of the mold and cured at room temperature for 24 h. Afterward, additional curing was performed in an oven at 40°C for four days. After fabrication and curing, the exterior surfaces of the specimen were carefully polished to obtain flat, smooth, and perfectly parallel surfaces. The smooth parallel surfaces enabled uniform compression loading along the fracture surface, avoided any stress concentration, and enabled the application of shear stresses parallel to the fracture. The final dimensions of the samples were 152.4-mm long, 127-mm wide, and 25.4-mm thick.

In addition to specimens fabricated with mated rough surfaces using sandpaper (Table 2), two additional mated-specimens were prepared. A flat fracture specimen and a replica specimen of a laboratory induced fracture. The specimen with the flat fracture surface was made using a plastic plate instead of sandpaper, and the replica specimen (GS01R specimen) was fabricated by casting gypsum against an induced fracture in granite.

Test specimens with nonmated fractures were fabricated using Lucite (i.e., acrylic material). Lucite was selected because of its well-known homogeneity and isotropy. Two prismatic Lucite blocks were fabricated with the same external dimensions as the gypsum blocks. The fracture surface roughness of each block was produced either by polishing (Lucite PL) or sandblasting (Lucite SB) with 25-μm grit.

## Surface roughness measurements

Before a specimen was mounted in a biaxial loading frame, the fracture surface roughness was measured in 250 μm increments in two orthogonal directions using a laser profilometer. The asperity height distributions for the samples are shown in Figure 3. The roughness distributions for the Lucite SB, gypsum flat, #220, #60, #36, and GS01R specimens are similar to a Gaussian distribution. The mean asperity and standard deviation of each specimen are summarized in Table . As listed in the table, fracture roughness (or asperity height) ranged roughly from 60 to 2870 μm. The roughness measurements of the Lucite PL (polished Lucite sample) were not made because the material was transparent and the laser was unable to focus on the surface of the specimen.

The fracture surface of the flat gypsum specimen had a mean asperity of 59–70 μm with 28 μm standard deviation, which is comparable to that for the gypsum #220. It was noted that the fracture plane of the flat gypsum specimen exhibited long-range waviness that resulted in a wider distribution for the asperity height, whereas the asperity height distribution was narrower for the gypsum #220 specimen which had a more planar surface and randomly distributed asperities.

**Table 2. Type of sandpaper and average grit size of the sandpaper used to create fracture roughness.**

| # of sandpaper | Average grit size of sandpaper (μm) | Sample name |
|---|---|---|
| #36 | 530 | Gypsum #36 |
| #60 | 265 | Gypsum #60 |
| #220 | 68 | Gypsum #220 |
| Flat plastic plate | — | Gypsum flat |

## Ultrasonic measurements

An ultrasonic array was used to acquire P- and S-wave signals transmitted across and reflected from the fractures (Figure 4). Thirteen broadband piezoelectric transducers with a central frequency of 1 MHz were housed in specially designed load platens that were placed on each side of the specimen. The transducer layout is shown in Figure 4 along with the polarization direction of S-wave transducers. The capital letters P and S represent P- and S-wave transducers, respectively. Using two different polarizations for the S-wave transducers enabled us to determine if the test specimen exhibited S-wave anisotropy. The intact Lucite and gypsum samples were determined to be isotropic.

The data acquisition system enabled the measurements of multiple transmitted and reflected full waveforms for postprocessing analysis. The system consisted of a chassis (PXI-1042) that contained a real-time onboard computer controller (PXI-8106) with two multiplexer matrix switches, a two channel 14-bit 100-MHz digitizer (PXI-5122) for acquiring full waveforms, two 10 channel power multiplexer (PXI-2585), and one multiplexer terminal block (TB-2630) for switching among multiple seismic sources and receivers.

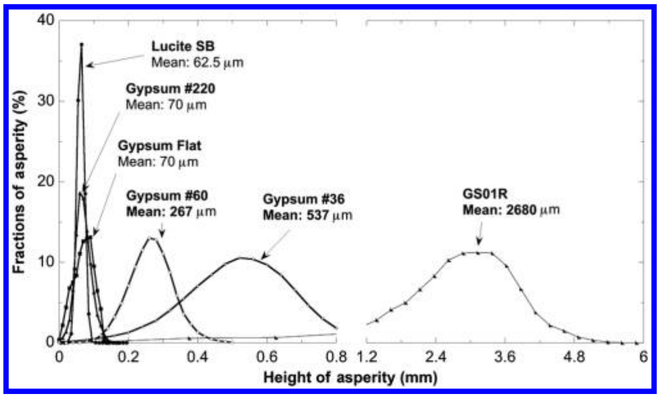


Figure 3. Surface roughness distribution of the fracture surfaces for Lucite SB, gypsum flat, #220, #60, #36, and GS01R specimens.

**Table 3. Measured mean asperity height and standard deviation in height for each specimen.**

| Fracture type | Sample name | Mean asperity (μm) | Standard deviation (μm) |
|---|---|---|---|
| Well-mated | GS01R | 2680–2870 | 878–887 |
| | Gypsum #36 | 335–537 | 65–67 |
| | Gypsum #60 | 265–267 | 64–67 |
| | Gypsum #220 | 62–70 | 22–23 |
| | Gypsum flat | 59–70 | 28 |
| Nonmated | Lucite SB | 62.5–106 | 10–18 |
| | Lucite PL | N/A | N/A |

A pulse generator was used to excite the transducers by 100-V square waves with a repetition rate of 5 kHz. Thirteen source-receiver pairs of transducers were used: three S-wave transducers (Panametrics V153) polarized parallel to the direction of shear, four S-wave transducers (Panametrics V153) perpendicular to the direction of shear, and six P-wave transducers (Panametrics V103) (Figure 4). The transducers were coupled to the surface using honey. The honey was baked in an oven at 90°C for 75 min to remove 8% of water. A thin plastic film was placed on the specimen to prevent the penetration of the honey into the pores of the specimen. A repeatability study on the effect of the thin plastic film and honey coupling was performed on an aluminum sample. The arrival times were repeatable to within 0.01 microsecond.

The sample and the platens containing the transducers were placed in a load frame under 1-MPa normal stress for 3 h to allow the couplant to equilibrate. This process resulted in stable, repeatable transmitted P- and S-wave signals. After 3 h, the load was removed and the experiments were performed for the five loading conditions shown in Figure 5a. A biaxial compression apparatus was used that consisted of two independent loading frames. A horizontal loading frame was used to apply a normal stress perpendicular to the fracture plane. A single axis Instron 444kN load frame, with an Instron model 59-R8100BTE controller running Bluehill 3 software was used to apply a shear stress parallel to the fracture plane. Mixed-mode biaxial loading conditions were chosen such that $\tau = \sigma \cdot \tan\,\theta$. The ratio of shear $\tau$ to normal stress $\sigma$ was given by $\tan\,\theta$, where $\theta = 5°, 15°, 30°$, and 40°. Uniaxial stress conditions are represented by $\theta = 0°$ when no shear load was applied (Choi, 2013; Hedayat, 2013).

## RESULTS AND ANALYSIS

In this section, the results from an experimental study are presented that show that the $\kappa_x/\kappa_z$ ratio depends on the geometric properties of the surfaces that compose the fracture and on the loading condition. First, the transmitted and reflected waves from an intact and fracture sample are shown for comparison. Followed by the spectral analysis technique used to determine changes in signal amplitude at a selected frequency. The $\kappa_x/\kappa_z$ ratio from the experimental data is then compared with the expected theoretical value from the displacement discontinuity model.

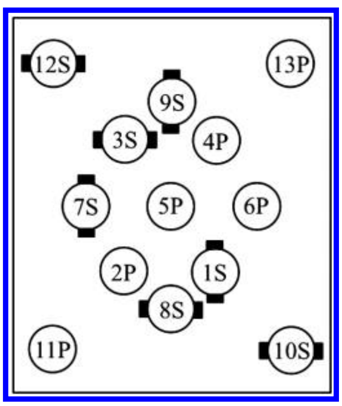


Figure 4. Transducer layouts. The elongated black box indicates the polarization direction of the S-wave transducers.

### Measurements of transmitted and reflected waveforms

Full-waveform measurements of transmitted and reflected P- and S-waves were made on the samples for the loading conditions given in Figure 5. The amplitude of the transmitted wave was greater than that from reflected wave as shown in Figure 6 for P-waves measured with P-wave transducer pair 2P-2P for gypsum #60 specimen. The peak-to-peak amplitude of the transmitted wave increased from 0.15 to 1.04 V (a factor of seven) over the range of applied normal stress (0.5–4.0 MPa), whereas the amplitude of the reflected wave only decreased by 13% over the same range of normal stresses. The increase in transmitted wave amplitude and the decrease in reflected-wave amplitude resulted from the increase in fracture specific stiffness with increasing load. The increase in fracture specific stiffness occurs from the increase in contact area between the two surfaces and decrease in fracture aperture (Pyrak-Nolte et al., 1987; Hopkins, 1990; Cook, 1992) that occurs as the sample is loaded. The increase in transmission occurs solely from changes in the fractures because the signal from the intact sample did not change with increasing normal load for either P- or S-waves on the Lucite samples or the gypsum samples (Choi, 2013; Hedayat, 2013).

The measured P- and S-wave velocities for the intact and fracture gypsum samples are shown in Figure 7 as a function of stress. For

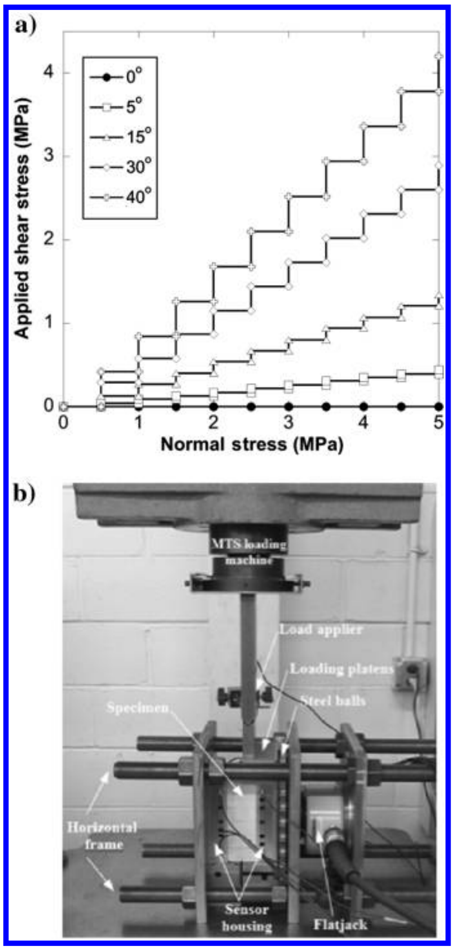


Figure 5. (a) Loading path of combined normal ($\sigma$) and shear ($\tau$) load ($\tau = \sigma \cdot \tan\,\theta$, $\theta = 0°, 5°, 15°, 30°$, and 40°) and (b) a photo of the biaxial apparatus.

the intact gypsum sample, the P-wave velocity ranged from 3138 to $3140 \pm 2$ m/s for a normal load that ranged from 0.5 to 4 MPa. The intact S-wave velocity was also constant ($1903–1905 \pm 2$ m/s) for the same load range. The $V_P$ and $V_S$ for the intact sample were insensitive to stress indicating that the intact gypsum does not contain any significant microcracks. For the fractured samples, the P-wave velocity was sensitive to the applied normal stress (Figure 7). The increase in P-wave velocity for the fracture gypsum samples ranged from 25 to 100 m/s as the load increased from 0.5 to 4 MPa except for fracture sample gypsum #220, in which the velocity increased only 5 to $7 \pm 2$ m/s over the same range of stresses. The S-wave velocities from the fractured gypsum samples increased by only 5 to $7 \pm 2$ m/s with increasing load (Figure 7).

## Spectral analysis

The P- and S-waves were first tapered to extract the first arrival from subsequent reflections. A comparison of the shape of the taper with the signal is shown in Figure 8 for P- and S-waves from the intact Lucite. The shape of taper was chosen to give the best representation of the spectral energy of the first arrival. The taper combined an open step function of 0.85-μs duration with one-half closing cosine of 1.71 μs. The selected taper was applied to the P- and S-waves. This taper isolated the initial signal from subsequent reflections and preserved the frequency content of the original signal without significant distortion of the high-frequency components. After applying the taper to the recorded signal, a fast Fourier transformation (FFT) was performed on the transmitted and reflected waves to obtain spectral amplitudes. An example of the spectra obtained from the tapered signals is shown in Figure 9 for the signals from intact Lucite given in Figure 8.

Given the spectral amplitudes obtained from the FFT, equation 18 was used to determine the fracture specific stiffness. The shear fracture specific stiffness is based on the measurements from the five S-wave transducers (1S, 3S, 7S, 8S, and 9S), and the normal fracture specific stiffness is based on data from the four P-wave transducers (2P, 4P, 5P, and 6P). The fracture specific stiffnesses were averaged to estimate the ratio of shear-to-normal fracture specific stiffness. The dominant frequency and wave velocity are listed in Table 1 for P- and S-waves for Lucite and gypsum.

## Stiffness ratio: Nonmated and well-mated fractures

### *Nonmated fractures*

The stiffness ratios $\kappa_x/\kappa_z$ of the nonmated fractures as a function of stress are shown in Figure 10 for the Lucite PL and SB specimens. For normal stresses greater than 1 MPa, $\kappa_x/\kappa_z$ was the same for both nonmated samples for all loading conditions ($\theta = 0°$, 5°,

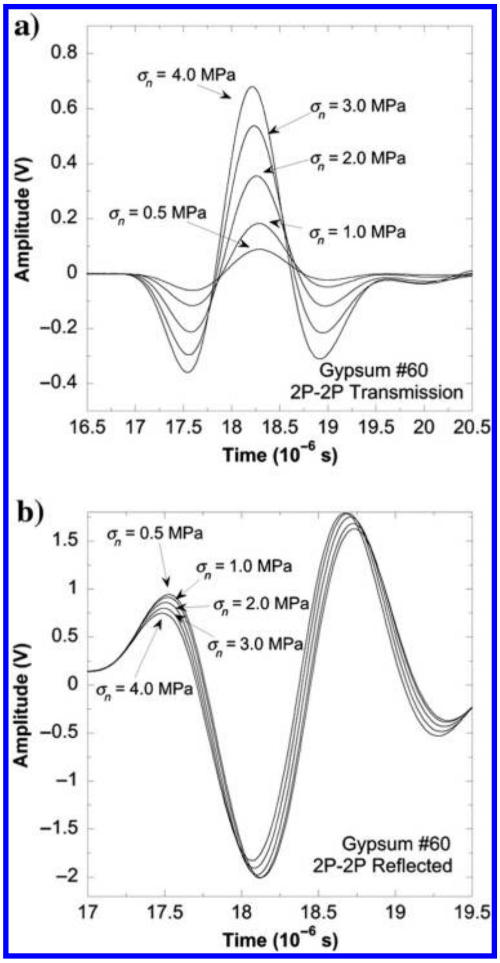


Figure 6. Recorded signals. (a) Transmitted and (b) reflected P-waves measured with transducer pair 2P-2P, for gypsum #60 specimen for normal stresses 0.5–4.0 MPa, for the 0° loading path.

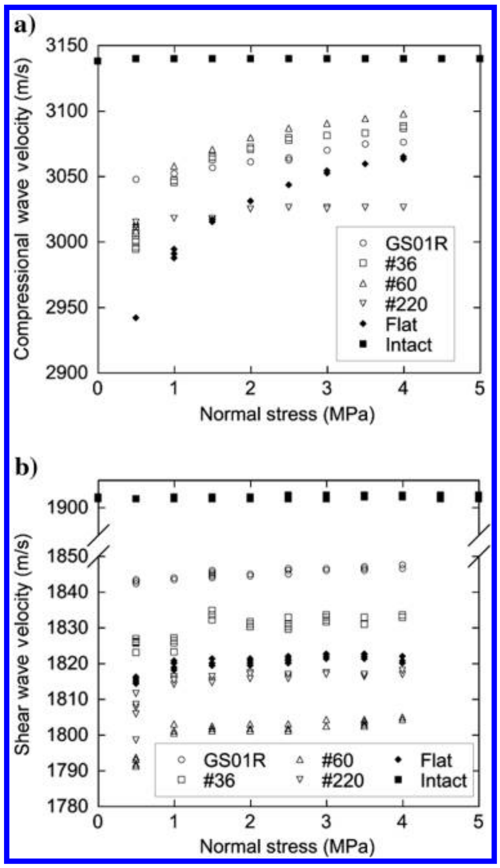


Figure 7. (a) The P- and (b) S-wave velocity as a function of normal stress for intact and fracture gypsum samples. Sample properties are listed in Tables 1–3.

15°, and 30°). The ratio approached asymptotically the theoretical ratio of 0.25 estimated from equation 17. The result indicates that, as the normal stress increased, the magnitude of the transmission coefficient of the P- and S-waves was equal.

However, the two nonmated samples exhibited different trends in $\kappa_x/\kappa_z$ at low-normal stresses (0–1.0 MPa) but was the same for all loading conditions ($\theta = 0°$, 5°, 15°, and 30°). The Lucite PL specimen approached the theoretical ratio by decreasing from an initial ratio of 1.2 at zero stress to 0.4 at a normal stress of 0.5 MPa. In contrast, for the Lucite SB specimen, the stiffness ratio gradually increased from a value of 0.2 at a normal stress of 0.5 MPa to the theoretical value. The difference in the $\kappa_x/\kappa_z$ at low stresses for samples Lucite PL and Lucite SB is attributed to the difference in surface preparation. Lucite PL was polished, whereas Lucite SB fracture surfaces were sandblasted. Above a normal load of 1 MPa, the $\kappa_x/\kappa_z$ ratio for both Lucite samples were close to the theoretical value, indicating that $T_P$ was approximately equal to $T_S$. Relatively smooth unmated surfaces with randomly distributed small asperity heights can be represented by the theoretical ratio for $\kappa_x/\kappa_z$ given by equation 18 in theoretical or numerical analyses for uniaxial and biaxial loading conditions.

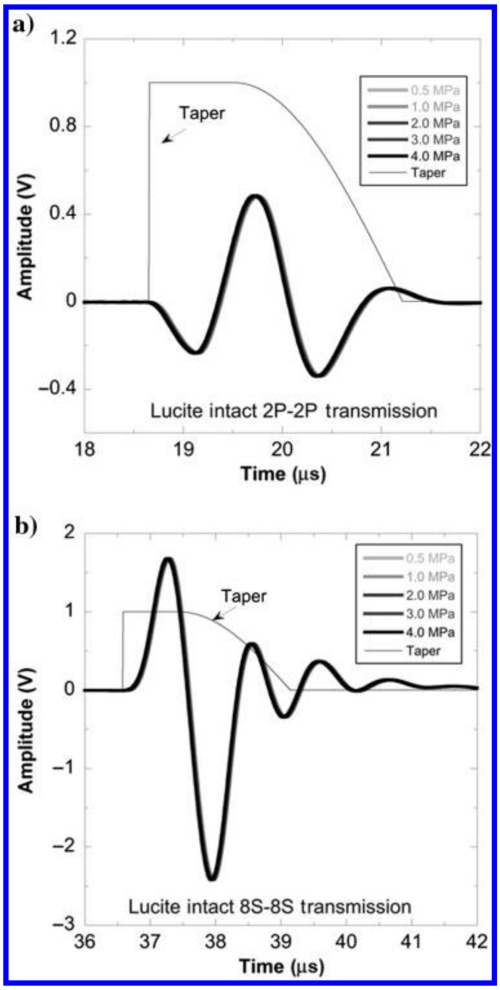


Figure 8. Recorded (a) P- and (b) S-wave signals on the intact Lucite sample using transducer pairs 2P-2P and 8S-8S, respectively. The taper used in the spectral analysis is also shown.

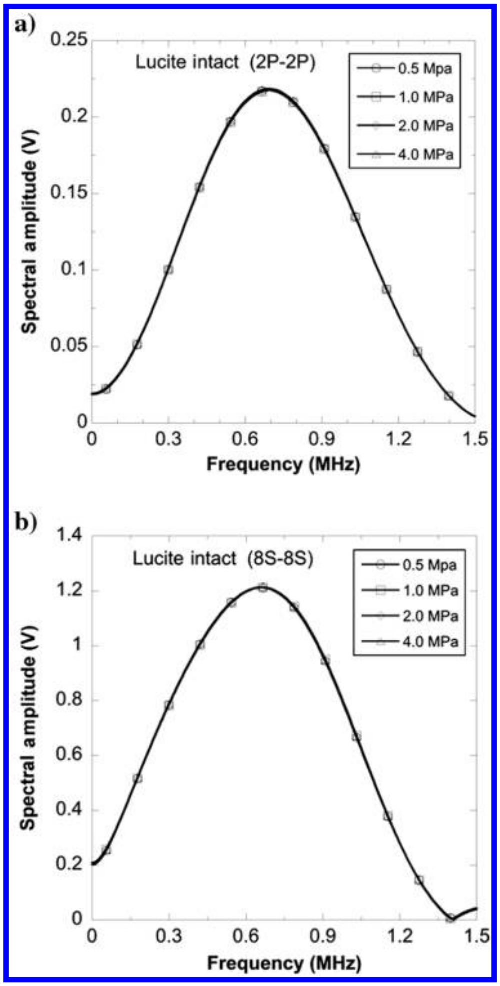


Figure 9. Spectra of the (a) P- and (b) S-wave signals shown in Figure 8 for the intact Lucite sample (for a range of normal stress 0.5–4 MPa) using transducer pairs 2P-2P and 8S-8S, respectively.

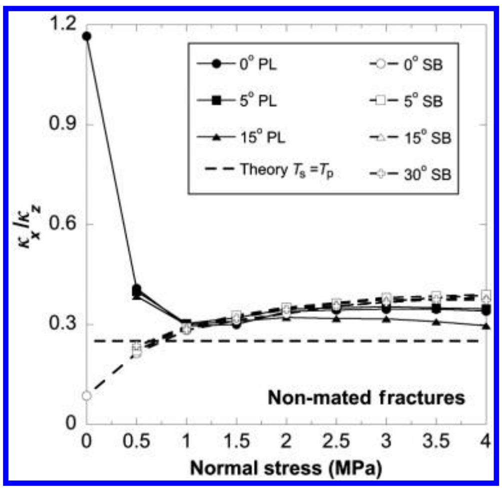


Figure 10. Variation of the ratio of shear-to-normal fracture specific stiffness $\kappa_x/\kappa_z$, as a function of normal stress $s$, for Lucite PL (solid lines) and Lucite SB (dashed lines) samples for different shear loading paths ($\tau = \sigma \cdot \tan\theta$, $\theta = 0°$, 5°, 15°, and 30°). The loading paths are shown in Figure 5a.

*Mated fractures*

The stiffness ratio $\kappa_x/\kappa_z$ of the well-mated gypsum specimens is shown in Figure 11 as a function of normal stress. For gypsum flat and #220 specimens, the stiffness ratio behaved in a manner similar to the nonmated fracture specimens Lucite PL and SB. For the gypsum flat specimen, the stiffness ratio decreased from 0.7–0.9 to 0.51–0.60 (with uncertainties of ±0.03 to ±0.04, respectively), whereas for the gypsum #220 specimen the stiffness ratio gradually increased with normal stress from approximately 0.2 to 0.39–0.61 (with uncertainties of ±0.06 to ±0.01, respectively). The major difference between the gypsum flat and gypsum #220 as well as the Lucite specimens is that the stiffness ratios from gypsum depended on shear stress. For example, the stiffness ratio of the gypsum #220 specimen increased from $0.39 \pm 0.06$ to $0.61 \pm 0.04$ over the normal stress range 3–4 MPa as the shear stress increased for loading paths 0°–30°.

The $\kappa_x/\kappa_z$ for the gypsum #60, #36, and GS01R specimens are shown in Figure 11b–11d, respectively. Under uniaxial loading conditions ($\theta = \theta°$), the stiffness ratio depended on stress. When subjected to mix-mode loading conditions ($\theta = 15°$–$40°$) and for normal stresses larger than 1.5 MPa, the $\kappa_x/\kappa_z$ for gypsum #60 and #36 specimens was independent of stress and the stiffness ratio was greater than the theoretical limit. As the proportion of shear load relative to the normal load increased, the $\kappa_x/\kappa_z$ ratio increased. For the replica sample GS01R, the $\kappa_x/\kappa_z$ ratio was almost stress independent under uniaxial loading conditions (0°).

The gypsum #60 specimen had stiffness ratios of $0.66 \pm 0.01$ for the 15° loading path, $0.86 \pm 0.01$ for the 30°, and $0.94 \pm 0.03$ for the 40° loading path, for normal stresses larger than 1.5 MPa. Similar observations were found for the gypsum #36 and GS01R specimens for the same range of normal stresses. The stiffness ratios obtained from the gypsum #36 specimen were $0.44 \pm 0.11$ for the 0° loading path, $0.70 \pm 0.08$ for the 15°, $0.93 \pm 0.02$ for the 30°, and $1.10 \pm 0.02$ for the 40° loading path. The GS01R specimen had stiffness ratios of $0.94 \pm 0.05$, $1.18 \pm 0.10$, and $1.47 \pm 0.05$ for the 15°, 30°, and 40° loading paths.

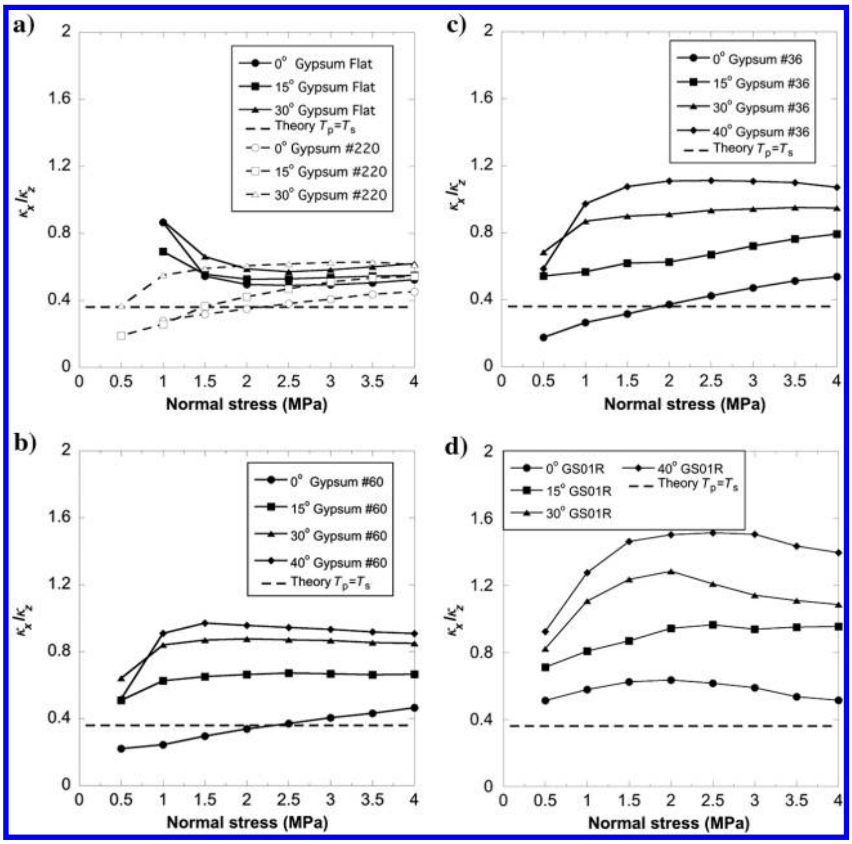


Figure 11. Ratio of shear-to-normal fracture specific stiffness $\kappa_x/\kappa_z$ from: (a) gypsum flat (solid lines) and #220 specimens (dashed lines), (b) #60 specimen, (c) #36 specimen, and (d) GS01R specimen as a function of normal stress $\sigma$ for different shear loading paths ($\tau = \sigma \cdot \tan\theta$, $\theta = 0°$, 5°, 15°, 30°, and 40°). The loading paths are shown in Figure 5a.

## DISCUSSION

The $\kappa_x/\kappa_z$ ratio for single fractures was examined for fractures with different surface roughness under uniaxial and mixed-mode loading condition. First, we discuss the stiffness ratio $\kappa_x/\kappa_z$ of the nonmated fracture in Lucite SB and the mated fracture in gypsum #220. These two specimens had comparable mean asperity sizes and standard deviations (Figure 3 and Table 3). The overall variation of the stiffness ratio of the nonmated and mated fractures with normal stress was approximately the same for these two samples. However, $\kappa_x/\kappa_z$ for gypsum #220 depended on the mixed-mode stress conditions (Figure 11a) but the ratio for Lucite SB did not (Figure 10). For stresses greater than 1.5 MPa, $\kappa_x/\kappa_z$, from the Lucite SB sample, equaled the theoretical limit and was the same for all mixed-mode loading conditions. The difference between the ratios for the two samples arises from the geometry of the two fractures and how this geometry deforms when subjected to normal and shear stresses.

Sandblasting tends to pit the surface of a material. When two sandblasted surfaces are brought into contact, voids are formed between flat contacts. The contact area is dominated by contacts that are parallel to the fracture plane while the voids are closer to the idealized penny-shaped crack geometry than a casted surface. As stress is applied to a sandblasted fracture, the increase in shear contact occurs mostly through the Poisson ratio effect along the flat asperities. The $\kappa_x$ and $\kappa_z$ for sandblasted surfaces are related through the Poisson ratio of the solid material, and the $\kappa_x/\kappa_z$ ratio is given by the theoretical limit and independent of mixed-mode loading conditions.

Casted surfaces, such as the gypsum #220 sample, have both normal and shear components of contact area. Numerical simulations have shown that the geometry of a fracture changes with increasing stress because deformation of the bulk material surrounding a fracture leads to mechanical interaction among contacting asperities (Hopkins, 1990, 2000). The resulting stiffness of a fracture depends on the 3D topography of the fracture void geometry that results from the roughness of the fracture surfaces and the spatial geometry of the contact area.

These effects are not captured by the idealized penny-shaped crack approach. Well-mated surfaces, like gypsum #220, produced more shear contacts between the two fracture surfaces with increasing stress than surfaces with random distributions of asperities like those in the sandblasted Lucite sample (SB). As the shear contact increases with increasing normal and shear stresses, the shear fracture stiffness also increases leading to a value of $\kappa_x/\kappa_z$ that is greater than the theoretical limit.

The comparison of the data from the fractures in Lucite SB and gypsum #220 indicates that the type of surface has an important effect on the stiffness ratio, even if the asperity size and distribution are comparable for both fracture surfaces. Random distributions of asperities produced by grinding, polishing, or sandblasting will approach the theoretical limit predicted by equation 18 under uniaxial and mixed-mode loading conditions. This is observed in the data of Lubbe et al. (2008) who measured normal and shear stiffnesses for synthetic fractures as a function of normal stress (uniaxial stress conditions) in Portland port freestone and carboniferous limestone. The Portland port freestone specimen was coarsely ground to a roughness of ±5 μm. The carboniferous limestone specimens had asperities of ±5 μm for coarsely ground, $2.72 \pm 0.2$ μm for ground, and $0.62 \pm 0.1$ μm for polished surfaces. The theoretical stiffness ratios for their samples ranged from 0.44 to 0.48 based on equation 18. The $\kappa_x/\kappa_z$ ratio based on Lubbe et al.'s (2008) data is shown in Figure 12 as a function of the applied normal stress along with the theoretical ratios. The trend in the $\kappa_x/\kappa_z$ values as a function of normal stress is similar to that observed for the Lucite SB sample under uniaxial stress conditions; i.e., $\kappa_x/\kappa_z$ approaches the theoretical limit with increasing stress.

As surface roughness increases for the well-mated fracture surfaces, the $\kappa_x/\kappa_z$ ratio was observed to be sensitive to the loading conditions. The shear fracture specific stiffness obtained from the gypsum #60 specimen is shown in Figure 13. The shear stiffness for uniaxial loading (0° loading path) was stress dependent and increased with increasing normal stress. Compared with the 0° loading path, the shear stiffness increased with increasing shear stress (from 15° to 40° loading). The dependency of shear stiffness on shear stress was observed for all of the well-mated fractures. The results for the well-mated fractures are consistent with the study of Pyrak-Nolte et al. (1996) that showed that shear stiffness increased when normal and shear stresses were applied to a fracture. They use fracture interface waves to determine the shear specific stiffness of three dolomite samples each containing a single fracture for uniaxial loading conditions, 0°, and mixed-mode loading conditions of 7.5°, 30°, and 52.5°. The fractures were induced using a technique similar to Brazil testing and resulted in well-mated fractures. They found that the shear stiffness increased faster with increasing normal load for mixed-mode loading conditions of 30° and 52.5° ($\tau \sim 0.58\sigma$ and $\tau \sim 1.3\sigma$) than under uniaxial conditions, 0°, and when small shear loads were applied (7.5° or $\tau \sim 0.13\sigma$). For example, they observe that the rate of change of shear specific stiffness with normal stress was three times higher under the 30° loading condition than for the uniaxial conditions. Pyrak-Nolte et al. (1996) hypothesize that the application of shear stress results in an increase in contact area along surfaces of the asperities that are orthogonal to the normal of the fracture plane, i.e., an increase in the shear contact in the fracture.

The experiments performed in this study and Pyrak-Nolte et al. (1996) suggest that increasing shear stress increases the shear contact area between the two fracture surfaces more than through the application of normal stress alone. For well-mated fractures, the measured $\kappa_x/\kappa_z$ ratio was only comparable or close to the theoretical limit for uniaxial loading conditions. For well-mated rough fractures, the $\kappa_x/\kappa_z$ ratio depends on the loading condition (e.g., uniaxial, biaxial, or mixed mode) and tends to asymptote to a constant $\kappa_x/\kappa_z$ ratio that is 2–4 times greater than the theoretical value.

The sensitivity of well-mated fractures to the applied shear stress is shown in Figure 14. The averaged stiffness ratios obtained from gypsum flat, #220, #60, #36, and GS01R are shown for loading paths 0°, 15°, 30°, and 40°. The average was obtained from the data for normal stresses greater than 1.5 MPa. As observed in Figure 14, the stiffness ratio depends on the relative magnitude of shear-to-normal stress (loading paths 0°, 15°, 30°, and 40°) and the roughness of the fracture surfaces. For example, for gypsum #36 specimen, the

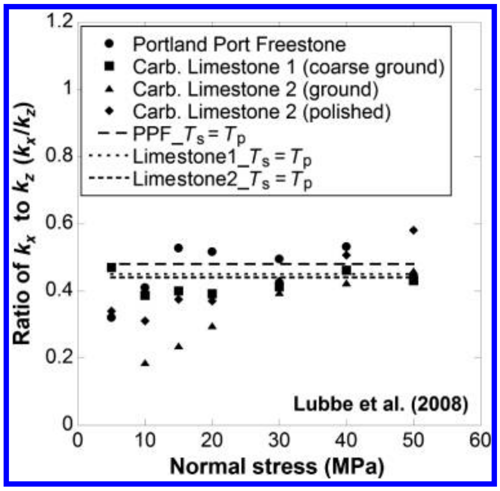


Figure 12. Ratio of shear-to-normal fracture specific stiffness obtained from the data in Lubbe et al. (2008). The ratios are compared with theoretical limit based on equation 18 (dotted lines).

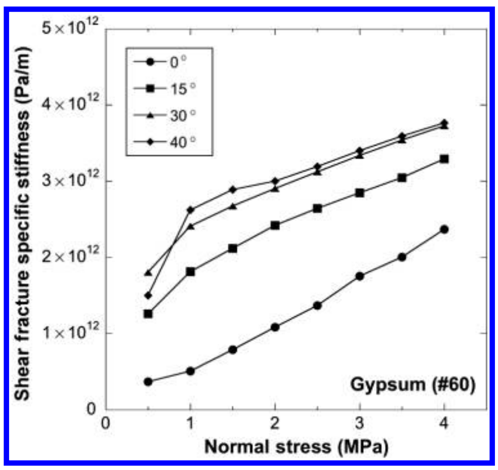


Figure 13. Shear fracture specific stiffness for the gypsum #60 specimen as a function of normal stress $\sigma$ for different shear loading paths ($\tau = \sigma \cdot \tan\theta$ for $\theta = 0°, 5°, 15°, 30°$, and 40°). The loading paths are shown in Figure 5a.

stiffness ratio increased from $0.44 \pm 0.11$ to $1.10 \pm 0.02$ with increasing shear stress (from 0° to 40° loading path). As the mean asperity size of the fracture increased from 62–70 μm (gypsum flat) to 2680–2870 μm (GS01R), the stiffness ratio obtained from the data for the 30° loading path increased from $0.60 \pm 0.04$ to $1.18 \pm 0.10$.

The sensitivity of the stiffness ratio to the shear stress for well-mated surfaces is a function of the fracture geometry. As noted, as the roughness of the fracture increases, the mean asperity sizes increases (Table 3) and the width of the asperity distribution increases (Figure 3). A microslope angle analysis was performed on the profilometry data from each surface and is shown in Figure 15. Park and Song (2013) define the microslope angle as the dip of the slope between neighboring asperities. A positive or negative angle represents an upward or downward slope, respectively. The width of the microslope distribution increased with increasing surface roughness. The smooth surfaces (gypsum flat and #220) contained slopes that ranged between ±5°, whereas the rough surfaces (gypsum #60 and #36) contained slope angles between ±20° and ±30°, respectively. In this study, surfaces with microslope angles >5° resulted in $\kappa_x/\kappa_z$ ratios that were greater than the theoretical limit. Surfaces with large microslope angles yield more shear contact than smooth surfaces. The asperity distribution and microslope analysis show that the details of the fracture geometry affect the $\kappa_x/\kappa_z$ ratio under mixed-mode loading conditions. The sensitivity of the $\kappa_x/\kappa_z$ ratio to shear stress depends on the number and orientation of shear contacts in the fracture.

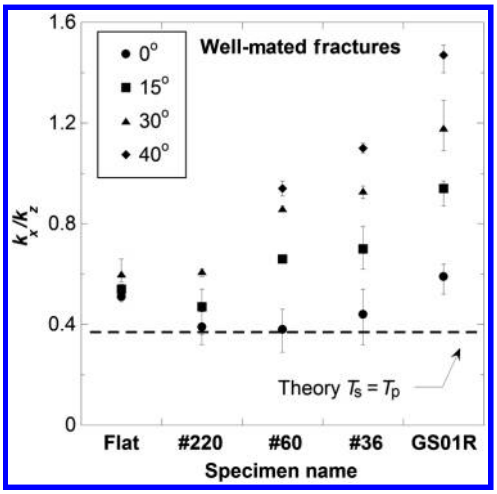


Figure 14. Stiffness ratio averaged over the range of normal stress of 1.5–4.0 MPa for the well-mated fracture specimens as a function of loading path ($\tau = \sigma \cdot \tan\theta$ for $\theta = 0°, 5°, 15°, 30°$, and 40°). The loading paths are shown in Figure 5a.

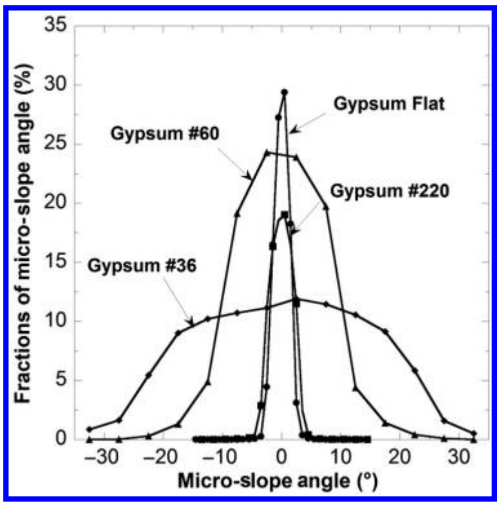


Figure 15. Distribution of microslope angle for the fracture gypsum samples.

## CONCLUSION

Whether or not the $\kappa_x/\kappa_z$ ratio is sensitive to loading conditions (e.g., uniaxial and biaxial) depends on the roughness of the fracture surfaces. For smooth fractures, the theoretical limit for $\kappa_x/\kappa_z$ derived from the displacement discontinuity theory held for mated/unmated surfaces and for all mixed mode and uniaxial loading conditions. However, this was not the case for rough fractures. The $\kappa_x/\kappa_z$ ratio for fractures composed of rough surfaces deviated from the theoretical limit, once the shear stress reached and/or exceeded ~25% of the normal stress. For high-shear loads (~80% of the applied normal stress), the $\kappa_x/\kappa_z$ for rough surfaces approached and exceeded $\kappa_x/\kappa_z \sim 1$.

Conventional mechanics approaches used to estimate fracture specific stiffness rely on elasticity and on the assumption that deformations depend on the stiffness of the rock. These assumptions result in a weak dependency of the $\kappa_x/\kappa_z$ on the Poisson's ratio, with values close to one and independent of the stress applied. Our experiments, together with laboratory and field observations from other researchers, indicate that these assumptions may not be correct and that normal and shear specific stiffnesses depend not only on the stiffness of the material that forms the fracture surfaces, but also on the surface type and roughness, i.e., the fracture void geometry. Hence, the conventional practice of assuming a constant stiffness ratio $\kappa_x/\kappa_z = 1.0$ may not be appropriate. Selecting a $\kappa_x/\kappa_z$ ratio for simulation of field conditions requires knowledge of the roughness of fracture surface and local stress conditions.

## ACKNOWLEDGMENTS

This research was supported by the National Science Foundation, Geomechanics and Geotechnical Systems Program, under grant no. CMS-0856296 and by the Geosciences Research Program, Office of Basic Energy Sciences United States Department of Energy (DE-FG02-09ER16022). This support is gratefully acknowledged.

## REFERENCES

Angus, D. A., J. P. Verdon, Q. J. Fisher, and J.-M. Kendall, 2009, Exploring trends in microcrack properties of sedimentary rocks: An audit of dry core velocity-stress measurements: Geophysics, **74**, no. 5, E193–E203, doi: 10.1190/1.3183940.

Bobet, A., and H. H. Einstein, 1998, Fracture coalescence in rock-type materials under uniaxial and biaxial compression: International Journal of Rock Mechanics and Mining Sciences, **35**, 863–888, doi: 10.1016/S0148-9062(98)00005-9.

Choi, M.-K., 2013, Characterization of fracture stiffness subjected to normal and shear stress: Ph.D. thesis, Purdue University.

Cook, N. G. W., 1992, Natural joints in Rock: Mechanical, hydraulic and seismic behavior and properties under normal stress, International Journal of Rock Mechanics and Mining Sciences and Gemechanics Abstracts, **29**, 198–223.

Far, M., 2011, Seismic characterization of naturally fractured reservoirs: Ph.D. thesis, University of Houston.

Far, M. E., J. J. S. de Figueiredo, R. R. Stewart, J. P. Castagna, D.-H. Han, and N. Dyaur, 2014, Measurements of seismic anisotropy and fracture

compliances in synthetic fractured media: Geophysical Journal International, **197**, 1845–1857, doi: 10.1093/gji/ggu101.
Gercek, H., 2007, Poisson's ratio values for rocks: International Journal of Rock Mechanics and Mining Sciences, **44**, 1–13, doi: 10.1016/j.ijrmms.2006.04.011.
Grechka, V., 2007, Multiple cracks in VTI rocks: Effective properties and fracture characterization: Geophysics, **72**, no. 5, D81–D91, doi: 10.1190/1.2751500.
Grechka, V., and M. Kachanov, 2006, Effective elasticity of fractured rocks: A snapshot of the work in progress: Geophysics, **71**, no. 6, W45–W58, doi: 10.1190/1.2360212.
Goodman, R. E., R. L. Taylor, and T. L. Brekke, 1968, A model for the mechanics of jointed rock: Journal of Soil Mechanics and Foundation Division, **94**, no. 3, Proc. Paper 5937, 637–659.
Gueguen, Y., and A. Schubnel, 2003, Elastic wave velocities and permeability of cracked rocks: Tectonophysics, **370**, 163–176, doi: 10.1016/S0040-1951(03)00184-7.
Hedayat, A., 2013, Mechanical and geophysical characterization of damage in rock: Ph.D. thesis, Purdue University.
Hobday, C., and M. H. Worthington, 2012, Field measurements of normal and shear fracture compliance: Geophysical Prospecting, **60**, 488–499, doi: 10.1111/j.1365-2478.2011.01000.x.
Hopkins, D. L., 1990, The effect of surface roughness on joint stiffness, aperture and acoustic wave propagation: Ph.D. thesis, University of California, Berkeley.
Hopkins, D. L., 2000, The implications of joint deformation in analyzing the properties and behavior of fractured rock masses, underground excavations and faults: International Journal of Rock Mechanics and Mining Sciences, **37**, 175–202, doi: 10.1016/S1365-1609(99)00100-8.
Hopkins, D. L., N. G. W. Cook, and L. R. Myer, 1987, Fracture stiffness and aperture as a function of applied stress and contact geometry: Presented at 28th U.S. Symposium on Rock Mechanics.
Hsu, C.-J., and M. Schoenberg, 1993, Elastic waves through a simulated fractured medium: Geophysics, **58**, 964–977, doi: 10.1190/1.1443487.
Hudson, J. A., 1981, Wave speeds and attenuation of elastic waves in material containing cracks: Geophysical Journal of the Royal Astronomical Society, **64**, 133–150, doi: 10.1111/j.1365-246X.1981.tb02662.x.
Hudson, J. A., E. Liu, and S. Crampin, 1997, The mean transmission properties of a fault with imperfect facial contact: Geophysics Journal International, **129**, 720–726, doi: 10.1111/j.1365-246X.1997.tb04507.x.
Jaeger, J. C., N. G. W. Cook, and R. W. Zimmerman, 2007, Fundamentals of rock mechanics: Blackwell Publishing.
Johnson, K. L., 1985, Contact mechanics: Cambridge University Press.
Park, J.-W., and J.-J. Song, 2013, Numerical method for the determination of contact areas of a rock joint under normal and shear loads: International Journal of Rock Mechanics and Mining Sciences, **58**, 8–22, doi: 10.1016/j.ijrmms.2012.10.001.
Kachanov, M., 1980, Continuum model of medium with cracks: Journal of the Engineering Mechanics Division of the American Society of Civil Engineers, **106**, 1039–1051.
Kachanov, M., R. Prioul, and J. Jocker, 2010, Incremental linear-elastic response of rocks containing multiple rough fractures: Similarities and differences with traction-free cracks: Geophysics, **75**, no. 1, D1–D11, doi: 10.1190/1.3268034.ARMA/USRMS 06-930.
Ko, T. Y., H. H. Markov, J. Einstein, and J. Kemeny, 2006, Crack Coalescence in Brittle Material under Cyclic Loading, 41st U.S. Symposium on Rock Mechanics, ARMA/USRMS 06-930.
Levin, V., M. Markov, and S. Kanaun, 2004, Effective field method for seismic properties of cracked rocks: Journal of Geophysical Research, **109**, B08202, doi: 10.1029/2003JB002795.
Liu, E., J. A. Hudson, and T. Pointer, 2000, Equivalent medium representation of fractured rock: Journal of Geophysical Research, **105**, 2981–3000, doi: 10.1029/1999JB900306.
Lubbe, R., J. Sothcott, M. H. Worthington, and C. McCann, 2008, Laboratory estimates of normal and shear fracture compliance: Geophysical Prospecting, **56**, 239–247, doi: 10.1111/j.1365-2478.2007.00688.x.
MacBeth, C., and H. Schuett, 2007, The stress dependent elastic properties of thermally induced microfractures in aeolian Rotliegend sandstone: Geophysical Prospecting, **55**, 323–332, doi: 10.1111/j.1365-2478.2007.00601.x.
Pervukhina, M., B. Gurevich, P. Golodoniuc, and D. N. Dewhurst, 2011, Parameterization of elastic stress sensitivity in shales: Geophysics, **76**, no. 3, WA147–WA155, doi: 10.1190/1.3554401.
Pyrak-Nolte, L. J., 1988, Seismic visibility of fractures: Ph.D. thesis, University of California.
Pyrak-Nolte, L. J., 1996, The seismic response of fractures and the interrelationships among fracture properties: International Journal of Rock Mechanics and Mining Sciences & Geomechanics Abstracts, **33**, 787–802, doi: 10.1016/S0148-9062(96)00022-8.
Pyrak-Nolte, L. J., L. R. Myer, and N. G. W. Cook, 1990, Transmission of seismic waves across single natural fractures: Journal of Geophysical Research, **95**, 8617–8638, doi: 10.1029/JB095iB06p08617.
Pyrak-Nolte, L. J., L.R. Myer, N. G. W. Cook, and P. A. Witherspoon, 1987, Hydraulic and mechanical properties of natural fractures in low permeability rock, *in* G. Herget, and S. Vongpaisal, eds., Proceedings of the Sixth International Congress on Rock Mechanics: A. A. Balkema, 225–231.
Pyrak-Nolte, L. J., S. Roy, and B. L. Mullenbach, 1996, Interface waves propagated along a fracture: Journal of Applied Geophysics, **35**, 79–87, doi: 10.1016/0926-9851(96)00009-2.
Rathore, J. S., E. Fjaer, R. M. Holt, and L. Renlie, 1995, P- and S-wave anisotropy of a synthetic sandstone with controlled crack geometry: Geophysical Prospecting, **43**, 711–728, doi: 10.1111/j.1365-2478.1995.tb00276.x.
Reyes, O., and H. H. Einstein, 1991, Failure mechanism of fractured rock: A fracture coalescence model: Proceedings of the Seventh International Congress of Rock Mechanics, 333–340.
Rice, J. R., 1979, Theory of precursory processes in the inception of earthquake rupture: Gerlands Beitrage Geophysik, **88**, 91–121.
Sayers, C. M., 1999, Stress-dependent seismic anisotropy of shales: Geophysics, **64**, 93–98, doi: 10.1190/1.1444535.
Sayers, C. M., and D.-H. Han, 2002, The effect of pore fluid on the stress-dependent elastic wave velocities in sandstones: 72nd Annual International Meeting, SEG, Expanded Abstracts, 1842–1845.
Sayers, C. M., and M. Kachanov, 1991, A simple technique for finding effective elastic constants of cracked solids for arbitrary crack orientation statistics: International Journal of Solids and Structures, **27**, 671–680, doi: 10.1016/0020-7683(91)90027-D.
Sayers, C. M., and M. Kachanov, 1995, Microcrack-induced elastic wave anisotropy of brittle rock: Journal of Geophysical Research: Solid Earth, 199, **100**, B3, 4149–4156, doi: 10.1029/94JB03134.
Sayers, C. M., A. D. Taleghani, and J. Adachi, 2009, The effect of mineralization on the ratio of normal to tangential compliance of fractures: Geophysical Prospecting, **57**, 439–446, doi: 10.1111/j.1365-2478.2008.00746.x.
Schoenberg, M., 1980, Elastic wave behavior across linear slip interfaces: Journal of the Acoustical Society of America, **68**, 1516–1521, doi: 10.1121/1.385077.
Schonberg, M., 1983, Reflection of elastic waves from periodically stratified media with interfacial slip: Geophysical Prospecting, **31**, 265–292, doi: 10.1111/j.1365-2478.1983.tb01054.x.
Shao, S., and L. J. Pyrak-Nolte, 2013, Interface waves along fractures in anisotropic media: Geophysics, **78**, no. 4, T99–T112, doi: 10.1190/geo2012-0464.1.
Shen, B., O. Stephansson, H. H. Einstein, and B. Ghahreman, 1995, Coalescence of fractures under shear stress experiments: Journal of Geophysical Research, **100**, 5975–5990, doi: 10.1029/95JB00040.
Takeuchi, K., 1991, Mixed-mode fracture initiation in granular brittle materials: M.S. thesis, Massachusetts Institute of Technology.
Verdon, J. P., D. A. Angus, J.-M. Kendall, and S. A. Hall, 2008, The effects of microstructure and nonlinear stress on anisotropic seismic velocities: Geophysics, **73**, no. 4, D41–D51, doi: 10.1190/1.2931680.
Verdon, J. P., and A. Wüstefeld, 2013, Measurement of the normal/tangential compliance ratio (ZN/ZT) during hydraulic fracture stimulation using shear wave splitting data: Geophysical Prospecting, **61**, 461–475, doi: 10.1111/j.1365-2478.2012.01132.x.
Wong, L. N. Y., and H. H. Einstein, 2006, Fracturing behavior of prismatic specimens containing single flaws, Presented at Golden Rocks 2006 41st U.S. Symposium on Rock Mechanics, ARMA/USRMS 06-899.
Worthington, M. H., and J. A. Hudson, 2000, Fault properties from seismic *Q*: Geophysical Journal International, **143**, 937–944, doi: 10.1046/j.1365-246X.2000.00315.x.